Ordering of the N-Terminus of Human MDM2 by Small Molecule Inhibitors

Klaus Michelsen,[†] John B. Jordan,[†] Jeffrey Lewis,[‡] Alexander M. Long,[§] Evelyn Yang,[‡] Yosup Rew,[∥] Jing Zhou,[⊥] Peter Yakowec,[#] Paul D. Schnier,[†] Xin Huang,*[,§] and Leszek Poppe*[,†]

[†]Molecular Structure & Characterization, Amgen, Inc., Thousand Oaks, California 91320, United States
[‡]Protein Technology, Amgen. Inc., Thousand Oaks, California 91320, United States
[§]Molecular Structure & Characterization, Amgen, Inc., Cambridge, Massachusetts 02139, United States
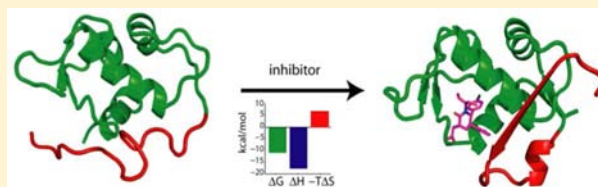[∥]Department of Medicinal Chemistry, Amgen, Inc., South San Francisco, California 94080, United States
[⊥]Molecular Structure & Characterization, Amgen, Inc., South San Francisco, California 94080, United States
[#]Protein Technology, Amgen, Inc., Cambridge, Massachusetts 02139, United States

ⓢ *Supporting Information*

ABSTRACT: Restoration of p53 function through the disruption of the MDM2-p53 protein complex is a promising strategy for the treatment of various types of cancer. Here, we present kinetic, thermodynamic, and structural rationale for the remarkable potency of a new class of MDM2 inhibitors, the piperidinones. While these compounds bind to the same site as previously reported for small molecule inhibitors, such as the Nutlins, data presented here demonstrate that the piperidinones also engage the N-terminal region (residues 10−16) of human MDM2, in particular, Val14 and Thr16. This portion of MDM2 is unstructured in both the apo form of the protein and in MDM2 complexes with p53 or Nutlin, but adopts a novel β-strand structure when complexed with the piperidinones. The ordering of the N-terminus upon binding of the piperidinones extends the current model of MDM2-p53 interaction and provides a new route to rational design of superior inhibitors.

INTRODUCTION

The MDM2 (murine double minute-2) protein is a negative regulator of p53, a tumor suppressor that activates transcription of genes involved in cell cycle arrest, apoptosis, senescence, and DNA repair. The design of MDM2 inhibitors that activate p53 tumor-suppressor activity by disrupting the MDM2-p53 complex has been a major pursuit in cancer research.[1,2] Competitively inhibiting protein−protein interactions (PPIs) with a small molecule poses a formidable challenge. Fortunately, for certain PPIs, particularly those that involve apoptotic proteins (i.e., Bcl-2, MDM2), it has been recognized that localized "hot spots" contribute significantly to the free energy of the interaction.[3,4] This facilitates the identification of potent inhibitors that are small enough to exhibit favorable drug properties.

Human MDM2 (491 residues, 55.2 kDa, UniProtKB Q00987) and p53 (393 residues, 43.7 kDa, UniProtKB P04637) interact primarily through their respective N-terminal regions; the transactivation domain (TAD) in the ordered N-terminal segment (residues17−26) of p53 protrudes into a hydrophobic pocket in the N-terminal domain (NTD) of MDM2.[1,5] Despite additional known MDM2-p53 interfaces,[6,7] the majority of drug discovery efforts to date have focused on disrupting the MDM2 NTD:p53 TAD interface (in short: MDM2-p53). In vivo studies with tumor xenografts demon-

strate that effective targeting of this interface enables p53-dependent inhibition of tumor growth.[8−10]

Molecular details of the MDM2−p53 interaction have been studied extensively by X-ray crystallography and NMR spectroscopy. Kussie et al. were the first to crystallize the complex and demonstrate how the p53 TAD (residues 17−26) interacts with the MDM2 NTD (residues 17−125) (PDB 1YCR). Three critical and nonreplaceable amino acids in the p53 TAD (Phe19-Trp23-Leu26) are observed,[11] which project into three hydrophobic grooves of MDM2 thus named as the Phe19, Trp23 and Leu26 pockets. This distinctive spatial presentation of hydrophobic groups is supported by a rigid α-helical scaffold, now believed to be a common binding motif among apoptotic proteins.[12,13] The most potent MDM2 inhibitors discovered to date all mimic these key hydrophobic interactions: the cis-imidizalones (Nutlins, Roche)[9] (PDB 1RV1, MDM2 a.a. 25−109), the benzodiazepinediones (J&J)[14] (PDB 1T4E, MDM2 a.a. 17−111), the chromeno-triazolopyrimidines (Amgen)[15] (PDB 3JZK, MDM2 a.a. 17−111), the imidazo-indoles (PDB 3LBK, MDM2 a.a. 18−111), spiro-oxindoles (University of Michigan)[16,17] (PDB 3LBL, MDM2 a.a. 18−111), and the meta-chloro piperidinones (Amgen)[10] (PDB 4ERE and 4ERF, MDM2 a.a. 17−111).

In addition to the classical hydrophobic triad, the amide of the spiro-oxindoles and the carboxylic acid of the piperidinones are hydrogen bonded to the Nε of His96. It was hypothesized that, due to this extra hydrogen bond, the piperidinones are 10−20 times more potent inhibitors of human MDM2 (residues 1−188) than other inhibitors such as Nutlin-3a.[10] In the present study, the piperidinones, but not p53 TAD (residues 17−26) or Nutlin-3a, exhibit a 10-fold increased potency against human and dog MDM2 (residues 1−188) as compared to mouse and rat MDM2 (residues 1−188), despite a greater than 90% sequence homology among the MDM2 proteins, including generally conserved residues compromising the Phe19, Trp23, and Leu26 pockets and His96. Until now, the molecular basis of the increased potency of the piperidinone inhibitors was not evident from existing structural data with the MDM2 a.a. 17−111 and a.a. 17−125 constructs.

Here, we present new binding and structural data describing the disruption of the MDM2−p53 interaction by the piperidinones. This class of inhibitors form additional van der Waals and hydrogen bond contacts with the N-terminal portion of human MDM2, specifically residues 6−16, which are absent in the endogenous MDM2−p53 interaction. X-ray and NMR structures of a longer human MDM2 construct (residues 6−125) reveal previously unobserved structural ordering of the N-terminal portion of MDM2 (residues 10−16) facilitated by piperidinone binding. We show that residues 10−25 of human MDM2 have an intrinsic propensity to form a highly ordered structural element (β-strand from a.a. 14−16, β-turn from a.a.17−20 and α-helix from a.a. 21−24) induced by the piperidinone inhibitors. These observations extend the N-terminal "lid" region (residues 16−24) of MDM2 described by Showalter[18] and McCoy et al.[19] and uncover a new "hot spot" for the development of novel, potent small molecule inhibitors of the human MDM2−p53 interaction.

■ EXPERIMENTAL SECTION

Synthesis of MDM2 Inhibitors. Pip-1, Pip-2 and Nutlin-3a were prepared as described in detail elsewhere.[9,10,20] Human p53 TAD (17−26) peptide was synthesized externally (Biopeptide Co., Inc.).

Generation of MDM2 and p53 Proteins. Full-length Human MDM2 for SPR studies was prepared externally (Boston Biochemicals). Human, dog, mouse and rat MDM2 (1−188) for SPR and HTRF studies were expressed as GST fusion proteins in *E. coli* and purified using glutathione affinity chromatography. Human MDM2 (2−118) and MDM2 (17−125) with and without a C-terminal AviTag were expressed and purified in a similar fashion for SPR and ITC studies, the GST-tag was removed and MDM2 was biotinylated specifically. Labeled (^{15}N, ^{13}C) and unlabeled Human MDM2 (6−125) for ITC, X-ray and NMR studies were expressed in *E. coli* with a His-tag and purified using a Ni-NTA column. Human, dog, mouse and rat AviTag p53 (1−83) for SPR and HTRF studies were expressed with a His-tag in *E. coli* and purified using Ni-NTA columns. Further details can be found in the Supporting Information.

Surface Plasmon Resonance (SPR) spectroscopy. SPR measurements were performed on a Biacore S51 instrument (GE Healthcare). Materials and reagents were purchased from GE Healthcare, Sigma-Aldrich or Thermo Scientific. CM5 chips were preconditioned using short pulses (2 × 6 s) of 100 mM HCl, 50 mM NaOH and 0.5% (v/v) SDS. Glutathione *S*-transferase (GST) or Streptavidin (SA) was immobilized at high density onto CM5 chips using amine coupling chemistry using a running buffer consisting of 10 mM HEPES pH 7.4 with 150 mM NaCl. For GST immobilization (15 000−17 000 RU): a 7 min EDC/NHS activation step [800 mM 1-ethyl-3-(3-dimethylaminopropyl) carbodiimide hydrochloride, 200 mM *N*-hydroxysuccinimide], 12 min 30 μg/mL goat anti-GST antibody (GE Healthcare) in 10 mM Na-acetate pH 5.0 and 7 min

1 M ethanolamine HCl pH 8.5. For SA immobilization (8000−10 000 RU): 15 min EDC/NHS activation, 15 min 0.5 mg/mL SA (Thermo Scientific) in 10 mM Na-acetate pH 5.0, 7 min 1 M ethanolamine HCl pH 8.5. For GST or AviTag, MDM2 capture buffer was replaced with a buffer made of 25 mM Tris-HCl, pH 7.5, 150 mM NaCl, 0.2 mM TCEP and 0.005% (v/v) Tween 20 (SPR buffer). The different MDM2 constructs (FL, 1−188, 2−118 and 17−125) were diluted in buffer (5−40 μg/mL) and captured onto either GST or SA surface (1400−2400 RU range). The binding experiments with p53 peptide and compound was conducted in the same buffer (with 5% (v/v) DMSO added) by diluting compound from a stock solution in DMSO down to desired concentration range and injecting sample over captured MDM2 surfaces for 2 min followed by a 3−4 min dissociation phase. All binding experiments were performed at least twice at 25 °C. The raw data was processed using Scrubber2 software (BioLogic Software Pty Ltd.) and the data kinetically fit to a 1:1 binding model which included a mass transfer limitation term.

Isothermal Titration Calorimetry (ITC). ITC experiments were performed on an Auto-ITC200 instrument (GE Healthcare). Human MDM2 (2−118), (6−125), and (17−125) protein was exchanged into SPR buffer using PD MiniTrap G-25 columns (GE Healthcare). Protein concentration was determined by absorbance at 280 nm using a molar extinction coefficient per cm of 10 430. For titration experiments, MDM2 protein was diluted to 5−10 μM and placed in the ITC cell. Human p53 peptide or compound in DMSO was diluted to 50−100 μM and placed in the syringe. Final DMSO concentration in the cell and syringe was 5% (v/v). Human p53 peptide and compound titration into buffer was also performed to ensure minimal heat of dilution. Titrations were performed at 25 °C using 2 μL injections (4 s duration, 180 s spacing, 5 s filter period). Reference power was set to 10 μcal/s and stirring speed to 1000 rpm. For proton linkage studies, the same buffer was used but with pH 7.0 and two additional buffers with different ionization enthalphy were included (phosphate and HEPES, pH 7.0). The raw data was baseline corrected and integrated using Origin 7.0. All thermodynamic parameters were obtained from the global fitting of the heat data assuming 1:1 interaction model, by optimization of reaction enthalpies, binding constants, ligands and proteins concentrations, and residual heats. The error limits were estimated from the Monte Carlo simulations assuming up to 5% errors in the pipetting. All the computations were performed using Matlab2011 (MathWorks, Inc.) software.

Homogeneous Time Resolved Fluorescence (HTRF). Monoclonal anti-GST antibody labeled with europium cryptate (Eu-anti-GST, 61GSTLB) and SA-Xl[ent!] (611SAXLB) were from Cisbio, the White 384 Opti plates used were from Perkin-Elmer and all other chemicals were from Sigma. The reaction buffer consisted of 1.06 mM KH$_2$PO$_4$, 2.96 mM Na$_2$HPO$_4$, 0.155 M NaCl, 0.1% (w/v) BSA and 1 mM DTT. One microliter of serial diluted inhibitor was transferred to 9 μL reaction buffer, and incubated with 10 μL of 1 nM human/dog/mouse or rat GST-MDM2 (1−188) for 20 min. Subsequently, 20 μL of 1.25 nM human/dog/mouse or rat avi-p53 (1−83) was added and incubated for 60 min before finally dispensing 10 μL of the detection mixture (1 nM SA-Xl[ent!], 3 nM Eu-anti-GST and 0.5 M KF). The plate incubated for 18 h was read on an Envision reader (Perken Elmer) using an excitation of 320 nm. The emissions were measured at 665 and 615 nm and the ratio of Em665/Em615 represented the MDM2−p53 interaction. Time-resolved fluorescence was measured with 50 flashes for both detectors with 60 μs delay after each excitation and a reading time of 300 μs. EC$_{50}$ values were established from duplicate measurements.

NMR Spectroscopy. NMR spectra were recorded at 15 °C on Bruker Avance III 500 and 800 MHz spectrometers (Bruker Biospin, Billerica, MA) equipped with triple-resonance TCI cryoprobes operating at 500.13 and 800.21 MHz for proton, respectively. Assignment of ^{1}H, ^{13}C, and ^{15}N resonances was achieved using a standard set of triple resonance experiments[21] along with an ^{13}C-HCCH-TOCSY[22] spectrum. All experiments were performed in 20 mM sodium phosphate, pH 7.0, 50 mM NaCl, 5 mM deuterated dithiothreitol (DTT-d_{10}) (Cambridge Isotopes, Cambridge, MA) and 90% H$_2$O/10% D$_2$O (except for the HCCH-TOCSY and isotope

filtered experiments, which were run in 99.996% D_2O). NOEs for ligand docking were obtained using a reduced dimensionality {3,2}-^{13}C/^{15}N-filtered NOESY-HSQC experiment (described further in Supporting Information).

All NMR data were processed using Topspin 3.0 or NMRPipe[23] and visualized using Sparky.[24] NMR structures were calculated in a semiautomated fashion using Cyana 3.0.[25] Protein structures were further refined in explicit water using Crystallography and NMR System (CNS).[26] The Ramachandran statistics for the final lowest-energy protein structure were determined using PROCHECK[27] and were as follows: most favored regions (59.9%), additionally allowed regions (37.5%), generously allowed regions (3.6%), and disallowed regions (0%). Ligand docking was performed using AMBER[28] and was done using 59 protein–ligand and 13 ligand–ligand NOEs. Further details can be found in the Supporting Information.

X-ray Crystallography. Crystals of MDM2 (6–125) with Pip-2 were obtained at 4 °C in hanging drops with 100 mM Citrate, pH 5.0, 1.5–2.0 M $(NH_4)_2SO_4$. These crystals belong to the space group C2 with unit cell parameters of a = 185.35, b = 73.95, c = 123.09 Å, and β = 121.60°. Diffraction data for all crystals in this work were collected on beamline 21-ID-F at the Advanced Photon Source (APS) and processed and scaled with HKL 2000. The cocrystal structure was solved by molecular replacement with PHASER using PDB entry code 1YCR as the template. Model building was carried out with QUANTA and refinement was done using CNS.

■ RESULTS

N-Terminal Residues 2–16 of MDM2 Contribute to Binding of the Piperidinones. The structures of the small molecule MDM2 inhibitors studied here are shown in Figure 1.
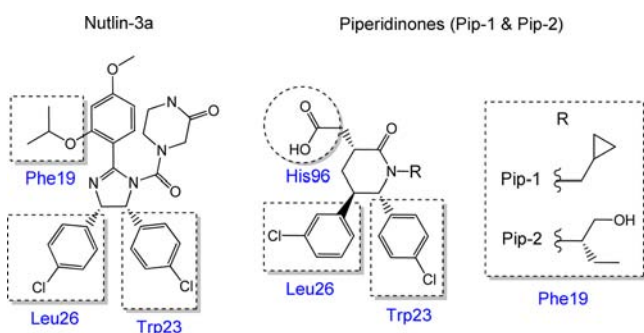

Figure 1. Chemical structure of small molecule MDM2 inhibitors studied. The boxes indicate the positions normally occupied by key p53 residues (Phe19-Trp23-Leu26). The piperidinones carboxy group (in the circle) makes an additional key contact with His96 not observed with p53 TAD peptide or Nutlin-3a compound.

They include two molecules from the piperidinone series,[10] the extensively studied Nutlin-3a,[9] and a short p53 TAD peptide (17–26). The binding kinetics and affinities were measured by Surface Plasmon Resonance (SPR) spectroscopy, where the full-length (FL) and truncated constructs (a.a. 17–125, 2–118) of human MDM2 were immobilized onto the sensor surface. With FL MDM2, all four inhibitors exhibited fast binding kinetics (Figure 2) with similar association rates (k_a values ~10^7 M^{-1} s^{-1}). Nutlin-3a and the most potent inhibitor, Pip-2, exhibited the slowest dissociation rate (k_d ~0.1 s^{-1}). The p53 peptide and Nutlin-3a bound all human MDM2 constructs equivalently (Table 1), within K_D ranges of 93–119 nM and 15.7–33 nM, respectively. This was consistent with previously reported observations that MDM2 residues 17–125 are necessary and sufficient for the interactions with these molecules.[5,9] More intriguing differences were observed with Pip-1 and Pip-2. These compounds bound to the shorter

construct (17–125) significantly weaker (>50-fold, see Table 1) than the longer construct, suggesting that additional residues besides His96 located within the N-terminal a.a. 1–16 or C-terminal a.a. 126–491 portion contribute to piperidinone binding. The similar affinities obtained for Pip-1 and Pip-2 with MDM2 FL and a.a. 2–118 (K_D range 22–27 nM for Pip-1 and 6.2–10.9 nM for Pip-2) confirmed that residues within the region of a.a. 2–16, and not 118–491, are engaged in Pip-1 and Pip-2 binding.

NMR and X-ray Structures of MDM2 (6–125) in Complex with the Piperidinones. The apo NMR structure of MDM2 (6–125) solved in-house was virtually identical to the published apo NMR structure (PDB 1Z1M, MDM2 a.a. 1–118).[29] We observed the same global fold and mostly disordered "lid" portion (residues 6–24), with an indication of a short α-helix formation between residues 21–24 (Figure 3). The quality of these structures was relatively low due to signal broadening of dynamic and unstructured portions of the MDM2 protein as well as protein precipitation. However, the NMR spectra improved significantly with the stoichiometric addition of Pip-1 to the MDM2 protein solution. The NMR spectra were of sufficient quality to obtain a well-defined structure of the MDM2/Pip-1 complex (Table 2). Figure 3 demonstrates the major structural changes in the MDM2 protein upon Pip-1 binding. These changes result in the ordering of the "extended lid" region into a well-defined short α-helix (residues 21–24) followed by a β-turn (residues 17–20) and short β-strand (residues 14–16) positioned closely to the inhibitor. A parallel crystallographic effort yielded crystals of MDM2 (6–125)/Pip-2 complex diffracting at 1.9 Å resolution with synchrotron radiation (Table 3). There were eight independent MDM2 (6–125)/Pip2 complexes in the crystal structure, highly similar to each other (with a backbone rmsd of 0.6 Å). The NMR and X-ray structure of the complexes were very similar, with subtle differences in the flexible loops (Figure S1) and a slight difference in the length of the β-strand formed by the N-terminal region.

The piperidinones bound in the "classical" manner by utilizing all three (Trp, Leu and Phe) pockets as described earlier with cocrystals of the MDM2 (17–111)/piperidinone complex.[10] The cyclopropyl moiety of Pip-1 and the ethyl moiety of Pip-2 were buried in the Phe19 pocket, and the para-chloro and meta-chloro-phenyl groups were buried in the Trp23 and Leu26 pockets, respectively. The carboxylic acid was also involved in hydrogen bond interaction with the Nε of His96.

However, structural comparison of the new MDM2 (6–125)/piperidinone complexes and the MDM2 (17–111)/piperidinone complex revealed one notable difference: the N-terminal residues in the MDM2 (6–125)/piperidinones complex were now structured, with residues 14–16 adopting a β-strand conformation and providing additional interactions with the piperidinones (Figure 4). The meta-chloro phenyl moiety of the piperidinone was buttressed between the side chains of Val14 and Thr16; the side chain oxygen of Thr16 was also hydrogen bonded to the Nε of His96 and positioned the Nε of His96 to form an optimal hydrogen bond with the carboxylic acid of the piperidinones. The same hydrogen bond also can be inferred from the MDM2/Pip-1 NMR structure. The hydrophobic interaction between Val14 and the meta-chloro phenyl moiety (as well as the para-chloro phenyl) of the piperidinones also appeared as a strong NOE contacts in the {3,2}-^{13}C/^{15}N-filtered NOSY-HSQC experiment (Figure 5).

17061

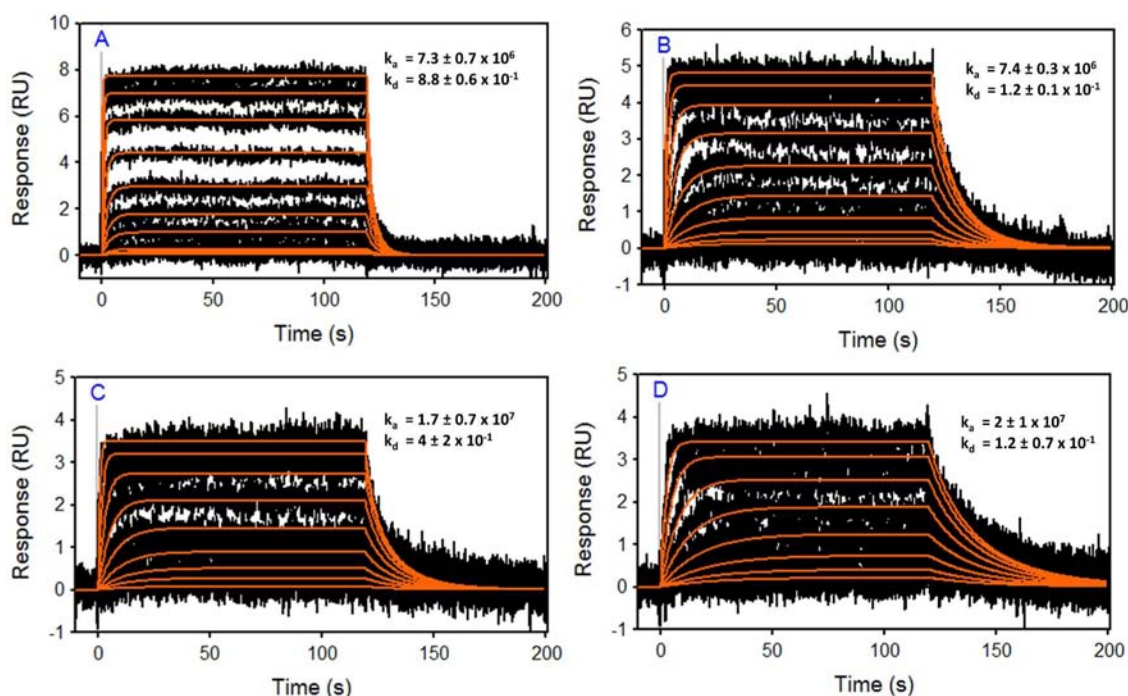dx.doi.org/10.1021/ja305839b | J. Am. Chem. Soc. 2012, 134, 17059–17067

Figure 2. Binding kinetics of inhibitors to full-length MDM2. Binding kinetics of p53 TAD peptide and small molecule MDM2 inhibitors to FL MDM2 measured by SPR spectroscopy. (A) p53 peptide (1, 0.50 μM, etc.), (B) Nutlin-3a (200, 100 nM, etc.), (C) Pip-1 (200, 100 nM, etc.), and (D) Pip-2 (50, 25 nM, etc.) binding to immobilized FL MDM2. Shown in black is the raw data and in red is the data fit. The association rate constant, k_a, is in $M^{-1} s^{-1}$ and dissociation rate constant, k_d, is in s^{-1}. The standard error was calculated from at least two separate measurements.

Table 1. SPR and ITC Data for the Different MDM2 Constructs[a]

inhibitor	binding attributes	FL	2−118	6−125	17−125
p53 peptide	SPR K_D (nM)	119 ± 2	118.7 ± 0.6	-	93 ± 9
	ITC K_D (nM)	-	112 ± 1	106 ± 1	111 ± 4
	ΔH (kcal/mol)	-	−11.9 ± 0.1	−11.7 ± 0.1	−12.1 ± 0.5
	$−T\Delta S$ (kcal/mol)	-	2.4 ± 0.1	2.2 ± 0.2	2.6 ± 0.5
Nutlin-3a	SPR K_D (nM)	15.7 ± 0.8	23 ± 3	-	33 ± 1
	ITC K_D (nM)	-	17.8 ± 0.8	24 ± 1	23.2 ± 0.8
	ΔH (kcal/mol)	-	−10.6 ± 0.5	−10.2 ± 0.5	−9.9 ± 0.4
	$−T\Delta S$ (kcal/mol)	-	0.03 ± 0.4	−0.2 ± 0.5	−0.5 ± 0.4
Pip-1	SPR K_D (nM)	22 ± 2	27 ± 5	-	1223 ± 277
	ITC K_D (nM)	-	17.7 ± 0.2	16.9 ± 0.2	563 ± 7
	ΔH (kcal/mol)	-	−16.3 ± 0.1	−15.9 ± 0.2	−10.1 ± 0.1
	$−T\Delta S$ (kcal/mol)	-	5.7 ± 0.2	5.3 ± 0.2	1.6 ± 0.1
Pip-2	SPR K_D (nM)	6.2 ± 2	10.9 ± 0.1	-	526 ± 138
	ITC K_D (nM)	-	8.2 ± 0.1	12.0 ± 0.1	210.7 ± 0.8
	ΔH (kcal/mol)	-	−17.5 ± 0.3	−17.6 ± 0.2	−10.0 ± 0.1
	$−T\Delta S$ (kcal/mol)	-	6.5 ± 0.3	6.8 ± 0.2	0.9 ± 0.1

[a]MDM2 inhibitors binding affinity to FL and various truncated human MDM2 constructs (2−118 and 17−125) were measured by SPR spectroscopy. ITC analysis was performed with truncated human MDM2 (2−118, 6−125 and 17−125). The standard errors for SPR measurements were calculated from at least two separate measurements, and for ITC measurements the errors were obtained from Monte Carlo simulations.

The MDM2 (6−125)/Pip-2 complexes exist as dimers in the crystal structure. The β-strand that corresponds to the residues 10−16 of one MDM2 (6−125)/Pip-2 complex forms an antiparallel β-sheet with the β-strand from another MDM2 (6−125)/Pip-2 complex (Figure S2). The dimer interface observed in the X-ray structures only buries 397 Å² of surface area and is not observed in solution NMR studies of the MDM2/Pip-1 complex. Self-association of MDM2, especially through interaction as an antiparallel β-strand, would be expected to cause at least small changes in the NH proton resonances of the residues involved. ¹⁵N HSQC spectra of this complex obtained at various concentrations (80 up to 800 μM, data not shown) did not exhibit any changes in chemical shifts. There is, however, a slight variation in the length of the newly formed N-terminal β-strand between the X-ray and NMR structures (residues 10−16 in X-ray and residues 14−16 in NMR) which could be due to the crystal packing and the presence of the dimer interface in the crystal structure. NMR chemical shift indices of the MDM2/Pip-2 complex also suggest that the β-strand secondary structure only comprises residues 14−16 in solution (Figure S3).
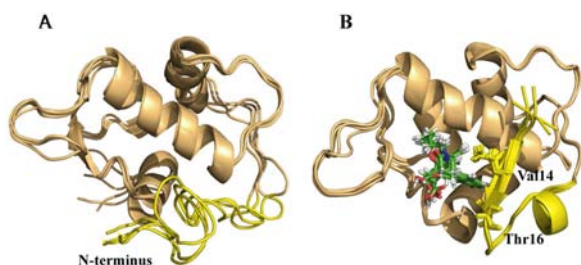
Figure 3. The NMR structures of apo human MDM2 (6−125) and Pip-1 with human MDM2 (6−125). The five lowest energy NMR structures of (A) Apo-MDM2 and (B) MDM2 bound to Pip-1 (in green). The regions highlighted in yellow correspond to the "extended lid", which comprises residues 11−24. In both structures, residues 6−10 remain disordered in solution and are thus truncated, along with the disordered C-terminus (residues 110−125) for clarity. The regions of disorder in the Apo structure adopt α-helical (residues 21−24) followed by a β-turn (residues 17−20) and β-sheet (residues 14−16) secondary structure in the inhibitor bound form. The side chains of Val14 and Thr16 are denoted in Panel B.

Table 2. NMR Refinement Statistics for MDM2 (6-125)/Pip-1 Structures

	MDM2(6−125)/Pip-1
NMR distance and dihedral constraints	
Distance constraints	
Total NOE	2612
Intraresidue	484
Inter-residue	
Sequential ($|i - j| = 1$)	653
Medium-range ($|i - j| < 4$)	717
Long-range ($|i - j| > 5$)	758
Intermolecular	59
Hydrogen bonds	62
Total dihedral angle restraints	142
ϕ	71
ψ	71
Structure statistics	
Violations (mean and SD)	
Distance constraints (Å)	0
Dihedral angle constraints (deg)	0
Max. dihedral angle violation (deg)	9.0
Max. distance constraint violation (Å)	0.4
Deviations from idealized geometry	
Bond lengths (Å)	5.37×10^{-3}
Bond angles (deg)	0.72
Impropers (deg)	2.65
Average pairwise rms deviation[a] (Å)	
Heavy	1.100
Backbone	0.637

[a]Pairwise rms deviation was calculated among 10 refined structures.

Residues 6−10 and 110−125 remained disordered in the NMR structure indicating, in agreement with the binding data, that these portions of the protein were not involved in any significant interactions with the rest of the complex. Through the use of the extended N-terminal construct, our model likely represents a complete contact map between piperidinones and the native MDM2 protein.

Table 3. X-ray Refinement Statistics for MDM2 (6-125)/Pip-2 Structure[a]

	MDM2(6−125)/Pip-2
Data collection	
Space group	$C2$
Cell dimensions	
a, b, c (Å)	185.35, 73.95, 123.09
α, β, γ (deg)	90.00, 121.60, 90.00
Resolution (Å)	50−1.90 (1.97−1.90)
R_{merge}	5.7 (49.3)
$I/\sigma I$	10.8 (2.7)
Completeness (%)	98.6 (97.6)
Redundancy	3.8 (3.8)
Refinement	
Resolution (Å)	50−1.90
No. reflections	109867
R_{work}/R_{free}	22.2/24.4
No. atoms	
Protein	13046
Ligand/ion	240
Water	866
B-factors	
Protein	29.1 Å^2
Ligand/ion	25.8 Å^2
Water	42.4 Å^2
Rms deviations	
Bond lengths (Å)	0.0089
Bond angles (deg)	1.44

[a]One crystal was used. Values in parentheses are for highest-resolution shell.
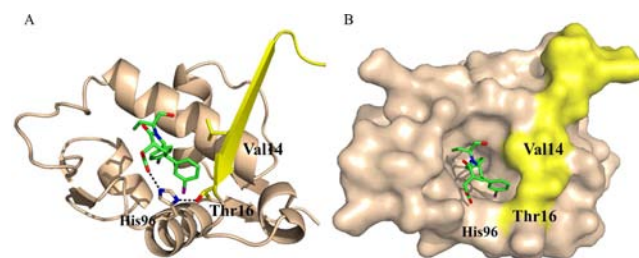

Figure 4. The crystal structure of Pip-2 with human MDM2 (6−125). (A) Shows a ribbon diagram representation of the complex. (B) Shows a surface representation of the complex. Pip-2 and the key residues in MDM2 are represented by sticks. Highlighted in yellow is the newly observed β-strand of the N-terminal portion. The carboxylic group of Pip-2 forms a hydrogen bond with His96, which in turn forms a hydrogen bond with Thr16. The meta-chloro phenyl moiety of Pip-2 is buttressed between the side chains of Val14 and Thr16, and picks up additional van der Waals interactions with human MDM2.

The Piperidinone−MDM2 Interaction Is Enthalpically Driven, but Entropically Unfavorable. To further characterize the interactions between the piperidinones and human MDM2, we carried out thermodynamic studies of Pip-1 and Pip-2 as well as the human p53 TAD peptide (a.a.17−26) and Nutlin-3a to various truncated forms of human MDM2 using isothermal titration calorimetry (ITC) (Table 1). The binding affinities obtained were consistent with those measured by SPR and validated the integrity of the human MDM2 (6−125) construct used for structural analysis (vide infra). The measured binding parameters (Table 1) for the p53 peptide
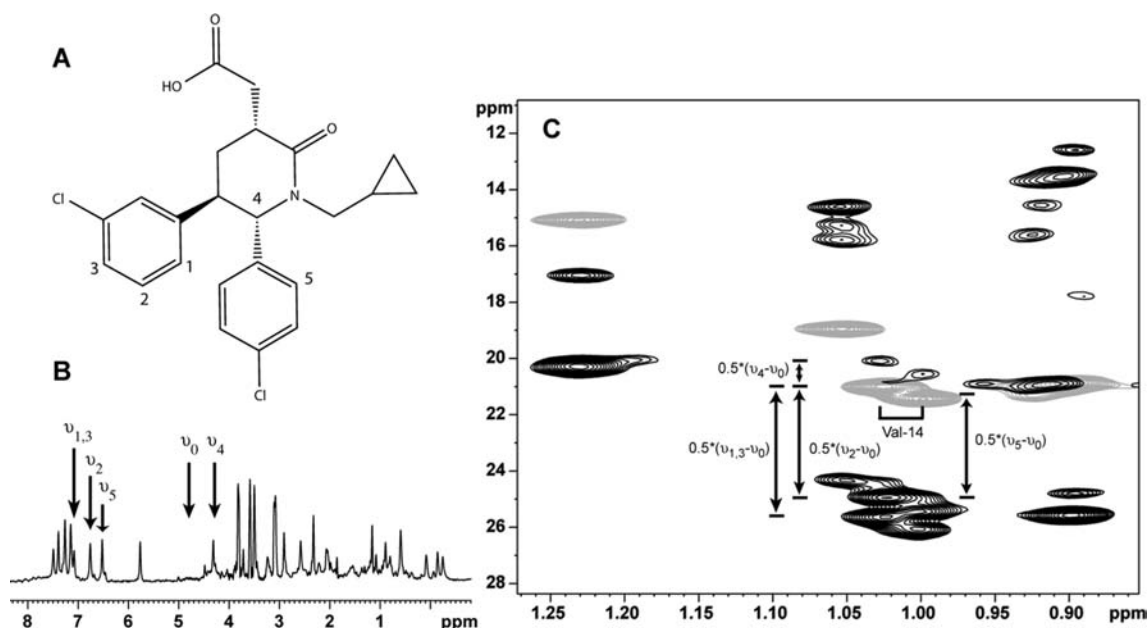
Figure 5. Pip-1 to MDM2 (6−125) NOEs from X-filtered {3,2}-NOESY-HSQC experiment. (A) The structure of the Pip-1 inhibitor and the corresponding protons (1−5) to which Val14 NOEs were observed. (B) Isotope filtered one-dimensional ^{1}H NMR spectrum of the ligand in the protein-bound state with v_0 marking the carrier frequency of the experiment (on water resonance), and v_1, v_2, v_3, v_4, and v_5 marking the frequencies of the nuclei shown in panel A. (C) Expansion of the methyl region of the {3,2}-X^5-NOESY-HSQC spectrum showing how the spectra (unmodulated and sine + cosine modulated) are used to determine ligand−protein NOEs. The lines shown mark the differences between the peaks in Hz, which can then be correlated back to the frequency of the ligand signals that give rise to the NOEs (shown in Panel B) as distances (in Hz) from the carrier frequency.
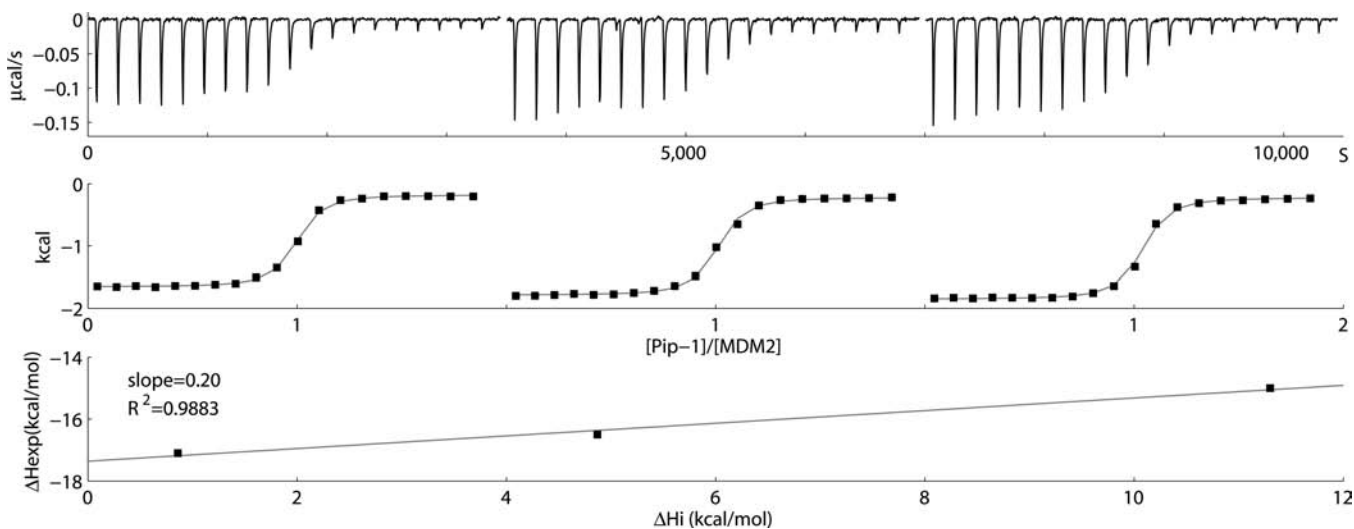

Figure 6. Proton linkage studies with Human MDM2 (6−125) and Pip-1. Measurements were performed in three buffers with different ionization enthalpies (from left to right: Phosphate, Hepes and Tris). Enthalpy, ΔH, from the global fit was plotted as a function of buffer ionization enthalpy ΔHi,[41] to obtain a ~0.2 proton transfer from solvent to complex.

and Nutlin-3a are similar for MDM2 (2−118), MDM2 (6−125) and MDM2 (17−125). In contrast, the two piperidinone inhibitors showed significant preference (>20 fold, see Table 1) for binding MDM2 (2−118) and MDM2 (6−125) in comparison to MDM2 (17−125). In the case of the p53 peptide, there was an entropic penalty of 2.2−2.6 kcal/mol likely associated with the adoption of α-helical conformation by the ligand.[18,30] For Pip-1 and Pip-2, there was a larger entropic penalty of 5.3−5.7 and 6.5−6.8 kcal/mol, respectively, associated with the ordering of N-terminal residues 11−24 of MDM2 observed in the NMR and X-ray complex structures,

but not in the apo NMR structure. In the case of piperidinones, the entropic penalty was outweighed by energetically favorable (large enthalpy) interactions of the piperidinone inhibitors with amino acids located on the β-strand portion of MDM2, particularly Val14 and Thr16 (via His96). The binding of Nutlin-3a did not involve any major structural changes,[18] and the entropic contribution to the free energy of binding, in this case, was negligible.

We also assessed enthalpic contributions of the proton transfer associated with the inhibitor binding (proton linkage) using ITC,[31] performed with MDM2 (6−125) in different

Table 4. Inhibitor Binding to MDM2 Proteins from Different Species[a]

inhibitor	assay	human	dog	mouse	rat
p53 peptide	K_D (nM)	125 ± 13	81 ± 2	44 ± 1	37 ± 11
	EC_{50} (nM)	52 ± 7	47 ± 8	45 ± 7	30 ± 3
Nutlin-3a	K_D (nM)	16 ± 3	18 ± 1	23.1 ± 0.7	20 ± 4
	EC_{50} (nM)	45 ± 2	46 ± 4	117 ± 2	84 ± 10
Pip-1	K_D (nM)	24 ± 3	33 ± 2	298 ± 62	318 ± 33
	EC_{50} (nM)	96 ± 3	112 ± 4	1175 ± 59	1157 ± 247
Pip-2	K_D (nM)	4.9 ± 0.7	11 ± 4	69 ± 16	70 ± 14
	EC_{50} (nM)	12.7 ± 0.3	26 ± 1	220 ± 33	223 ± 42

[a]Affinities to human, dog, mouse and rat MDM2 (1−188) were measured by SPR spectroscopy. The disruption of human, dog, mouse and rat MDM2 (1−188):p53 (1−83) interaction by human p53 (17−26) peptide and compounds was measured using HTRF assay. The standard deviation was calculated from at least two separate measurements.

buffers, widely ranging in the ionization enthalpies. Pip-1 showed small proton linkage at pH 7, corresponding to ~0.2 protons transferred from the solvent to the complex (Figure 6). The positive proton linkage was likely associated with the protonation of the Nε of His96, which became positively charged in the complex and interacted favorably with the negatively charged carboxylic group on the piperidinones.

Binding of Piperidinones to MDM2 Proteins of Nonhuman Origin. To investigate the difference in potency of the piperidinones against human/dog and mouse/rat MDM2 (1−188) and to elucidate the importance of the residues involved in the interaction between piperidinones and MDM2, we carried out binding studies of the two piperidinones as well as the human p53 peptide (17−26) and Nutlin-3a to human, dog, mouse and rat MDM2 (a.a. 1−188) using SPR (Table 4). We also tested the competing efficiency of each ligand in a Homogeneous Time Resolved Fluorescence (HTRF) assay, which quantified the effective concentration of a ligand needed to disrupt 50% of the MDM2 (a.a. 1−188)/p53 (a.a. 1−83) complex from human, dog, mouse and rat (Table 4)

The MDM2 (a.a. 1−188) sequence homology for these species was high (>90% similarity, Figure S4), while for p53 (a.a. 1−83), the homology was somewhat lower (75−83% similarity, Figure S5), but higher for p53 (a.a. 17−26) (>90% similarity with other 3 species). From the SPR data in Table 4, it was clear that 10-fold increase in potency for the piperidinones against human and dog MDM2 was the result of differences in MDM2 and not p53. To address this matter, we looked at sequence variability in MDM2 among the four species studied and performed site directed mutagenesis studies on human MDM2. On the basis of the structural data presented here, the residues forming critical interactions with the piperdinone inhibitors were conserved between all four species, with the exception of residue 14 in the N-terminus and residues 54 and 57 in the p53 binding pocket (Figure S4). Residue 54, a leucine in human MDM2, was an isoleucine in the dog, rat, and mouse variants. This negated the need to make mutants for position 54, since all other critical residues were conserved in human and dog. However, the human protein possessing the L57I mutation exhibited little or no effect on the binding of human p53 (a.a. 17−26) or Nutlin-3a and resulted in two to four-fold decrease in the affinity of the piperidinones (Table 5). Also, residue 14 in the N-terminal region exhibited variability in the human/dog and rat/mouse species (valine or alanine, respectively). The V14A mutation (and the double mutation V14A, L57I) was used to investigate the role of this residue in binding to the p53 peptide, Nutlin-3a, Pip-1, and Pip-2. As expected, this single mutation had no measurable effect on the

Table 5. Inhibitor Binding to Human MDM2 Mutants[a]

inhibitor	WT	V14A	L57I	V14A,L57I
p53 peptide	129 ± 0.2	120 ± 0.6	173.5 ± 0.4	127 ± 3
Nutlin-3a	9.5 ± 0.4	10.8 ± 0.3	23.4 ± 0.8	15.8 ± 0.1
Pip-1	20.7 ± 0.9	18.2 ± 0.9	80 ± 4	47 ± 2
Pip-2	10 ± 1	13 ± 1	35.6 ± 1.0	25.8 ± 0.2

[a]Binding affinities (K_D in nM) of MDM2 inhibitors to human MDM2 (2−118) WT and mutants were measured by SPR spectroscopy. The standard deviation was calculated from at least two separate measurements.

binding affinity of human p53 peptide and Nutlin-3a, but surprisingly had no effect on the binding of the piperidinones. Therefore, it seems that a combination of changes in amino acids, most likely involving residues not in direct contact with the piperidinone inhibitors, is responsible for the observed differences in potency between species.

■ DISCUSSION

The new class of piperidinone inhibitors of the MDM2-p53 protein−protein interaction mimics the classical hydrophobic triad Trp-Leu-Phe from the p53 TAD binding domain. In addition, the piperidinones favorably interact with the N-terminus of human MDM2, despite the entropic cost paid to order this flexible region of the apo structure. Hence, the new piperidinones have overcome the enthalpy−entropy compensation confinement, a known conundrum in many campaigns of rational inhibitor design.[32] Interestingly, the involvement of the N-terminus in the binding of MDM2 inhibitors was previously suggested based on semiempirical interaction models built from a set of structure−actitivty data on MDM2 inhibitors.[33] Our study, based on biophysical and structural data, extends the function of the N-terminal "lid" portion of MDM2 past what has been described in previous studies of shorter MDM2 constructs (residues17−111/125) bound to the p53 peptide and Nutlins.[18,19,30] In the case of the piperidinone inhibitors, the "extended lid" is structured, and engages additional residues in the MDM2 N-terminus (residues 10−16), which have been truncated in most of published X-ray and NMR studies. The U-shaped N-terminus (a.a. 11−24) of MDM2 consists of a short β-strand (a.a. 14−16) followed by a β-turn (a.a. 17−20) and short α-helix (a.a. 21−24) supported by the inhibitor. The 6−16 amino acid portion, disordered in the apo form and when bound to most inhibitors, likely contributes to problems with protein stability and crystallizability of apo-MDM2, as crystal structures of MDM2 with more truncated N-terminal regions are more readily obtainable (i.e., residues 17−111/125).

There is an intriguing difference in binding of the piperidinones to MDM2 proteins from human and dog vs mouse and rat. In human and dog MDM2, the N-terminus contributes 2 kcal/mol to the free energy of the piperidinone binding. This contribution, however, appears to be significantly diminished (by 1 kcal/mol) in the case of mouse and rat MDM2, and is practically absent in case of p53 peptide and Nutlin-3a binding. Although a structural explanation for the differences in potency between species is not available at the present time, based on the site directed mutagenesis data, it is plausible that the piperidinones still engage the N-terminus of mouse and rat MDM2, although maybe not as efficiently from the perspective of enthalpy−entropy compensation as in the case of human MDM2. In support of this hypothesis, secondary structure predictions suggest that the propensity for β-sheet formation in the N-terminal portion of the human and dog MDM2 seems to be encoded in the primary amino acid sequence. An *ab initio* secondary structure prediction from the first N-terminal 30 amino acids (Figure S6) exhibited a clear preference for the formation of an extended β-strand type structure between residues 14−16 in human and dog MDM2 (consistent with NMR structures), but favored a random coil in the case of the rat and mouse variants. The short α-helix was predicted between residues 21−24 in all four species investigated, and has been previously observed in experimental complex structures with the shorter MDM2 (residues 17−111/125) constructs (i.e., PDB 1T4E). The fast association rate observed with the piperidinones and human FL MDM2 must also involve fast conformational rearrangement of the N-terminal portion upon the inhibitor binding, consistent with its intrinsic structural propensity.

Notably, the piperidinones appeared to be ineffective (EC_{50} values in the HTRF assay were greater than 30 μM) in disrupting the homologous MDMX (MDM4)/p53 interaction.[34] Although the N-terminal domains of the MDM2 and MDMX proteins are structurally[35] and dynamically[36] similar, the amino acid differences in the hydrophobic pockets and in the N-terminus are even more pronounced than the differences within the MDM2 proteins of different species. In the case of the p53 peptide and Nutlin-3a inhibitor, the differential binding to the human MDM2 and MDMX proteins has been well rationalized in terms of the canonical hydrophobic interactions.[37−39] The engagement of the N-terminus as observed here with piperidinones adds an additional dimension to the inhibitor specificity and likely renders dual MDM2/MDMX inhibition even more challenging than currently anticipated.[40]

In summary, we have explored new structural features of the human MDM2 protein associated with the N-terminal region that may offer a novel strategy for extending the target interface for drug interactions with this protein. This may lead to more specific and potent drugs to disrupt MDM2−p53 interactions, thereby sustaining p53's antiproliferative activity.

ASSOCIATED CONTENT

Ⓢ Supporting Information

Overlay of NMR and X-ray structure, MDM2 (6−125)/Pip-2 dimer observed in the crystal structure, chemical shift indices of Apo- and Holo-MDM2/Pip-1, sequence homology between human, dog, mouse and rat MDM2 (1−188) and p53 (1−83), secondary structure predictions within N-terminal region of MDM2, {3,2} $^{13}C,^{15}N$ filtered NOESY-HSQC pulse sequence and NMR experimental details as well as detailed protocols for protein generation. The atomic coordinates of the crystal and NMR structures have been deposited into Protein Data Bank with PDB access codes 4HBM and 2LZG respectively. The NMR chemical shifts and NMR constraints have been deposited into BioMagResBank with BMRB accession number 18755. This material is available free of charge via the Internet at http://pubs.acs.org.

AUTHOR INFORMATION

Corresponding Author

hxin@amgen.com; lpoppe@amgen.com

Notes

The authors declare no competing financial interest.

REFERENCES

(1) Oliner, J. D.; Pietenpol, J. A.; Thiagalingam, S.; Gyuris, J.; Kinzler, K. W.; Vogelstein, B. *Nature* **1993**, *362*, 857−860.

(2) Klein, C.; Vassilev, L. T. *Br. J. Cancer* **2004**, *91*, 1415−1419.

(3) Wells, J. A.; McClendon, C. L. *Nature* **2007**, *450*, 1001−1009.

(4) Yin, H.; Hamilton, A. D. *Angew. Chem., Int. Ed.* **2005**, *44*, 4130−4163.

(5) Kussie, P. H.; Gorina, S.; Marechal, V.; Elenbaas, B.; Moreau, J.; Levine, A. J.; Pavletich, N. P. *Science* **1996**, *274*, 948−953.

(6) Haupt, Y.; Maya, R.; Kazaz, A.; Oren, M. *Nature* **1997**, *387*, 296−299.

(7) Poyurovsky, M. V.; Katz, C.; Laptenko, O.; Beckerman, R.; Lokshin, M.; Ahn, J.; Byeon, I. J.; Gabizon, R.; Mattia, M.; Zupnick, A.; Brown, L. M.; Friedler, A.; Prives, C. *Nat. Struct. Mol. Biol.* **2010**, *17*, 982−989.

(8) Shangary, S.; Qin, D.; McEachern, D.; Liu, M.; Miller, R. S.; Qiu, S.; Nikolovska-Coleska, Z.; Ding, K.; Wang, G.; Chen, J.; Bernard, D.; Zhang, J.; Lu, Y.; Gu, Q.; Shah, R. B.; Pienta, K. J.; Ling, X.; Kang, S.; Guo, M.; Sun, Y.; Yang, D.; Wang, S. *Proc. Natl. Acad. Sci. U.S.A.* **2008**, *105*, 3933−3938.

(9) Vassilev, L. T.; Vu, B. T.; Graves, B.; Carvajal, D.; Podlaski, F.; Filipovic, Z.; Kong, N.; Kammlott, U.; Lukacs, C.; Klein, C.; Fotouhi, N.; Liu, E. A. *Science* **2004**, *303*, 844−848.

(10) Rew, Y.; Sun, D.; Gonzalez-Lopez De Turiso, F.; Bartberger, M. D.; Beck, H. P.; Canon, J.; Chen, A.; Chow, D.; Deignan, J.; Fox, B. M.; Gustin, D.; Huang, X.; Jiang, M.; Jiao, X.; Jin, L.; Kayser, F.; Kopecky, D. J.; Li, Y.; Lo, M. C.; Long, A. M.; Michelsen, K.; Oliner, J. D.; Osgood, T.; Ragains, M.; Saiki, A. Y.; Schneider, S.; Toteva, M.; Yakowec, P.; Yan, X.; Ye, Q.; Yu, D.; Zhao, X.; Zhou, J.; Medina, J. C.; Olson, S. H. *J. Med. Chem.* **2012**, *55*, 4936−4954.

(11) Bottger, A.; Bottger, V.; Garcia-Echeverria, C.; Chene, P.; Hochkeppel, H. K.; Sampson, W.; Ang, K.; Howard, S. F.; Picksley, S. M.; Lane, D. P. *J. Mol. Biol.* **1997**, *269*, 744−756.

(12) Ha, J. H.; Won, E. Y.; Shin, J. S.; Jang, M.; Ryu, K. S.; Bae, K. H.; Park, S. G.; Park, B. C.; Yoon, H. S.; Chi, S. W. *J. Am. Chem. Soc.* **2011**, *133*, 1244−1247.

(13) Shin, J. S.; Ha, J. H.; He, F.; Muto, Y.; Ryu, K. S.; Yoon, H. S.; Kang, S.; Park, S. G.; Park, B. C.; Choi, S. U.; Chi, S. W. *Biochem. Biophys. Res. Commun.* **2012**, *420*, 48−53.

(14) Grasberger, B. L.; Lu, T.; Schubert, C.; Parks, D. J.; Carver, T. E.; Koblish, H. K.; Cummings, M. D.; LaFrance, L. V.; Milkiewicz, K. L.; Calvo, R. R.; Maguire, D.; Lattanze, J.; Franks, C. F.; Zhao, S.; Ramachandren, K.; Bylebyl, G. R.; Zhang, M.; Manthey, C. L.; Petrella, E. C.; Pantoliano, M. W.; Deckman, I. C.; Spurlino, J. C.; Maroney, A. C.; Tomczuk, B. E.; Molloy, C. J.; Bone, R. F. *J. Med. Chem.* **2005**, *48*, 909−912.

(15) Allen, J. G.; Bourbeau, M. P.; Wohlhieter, G. E.; Bartberger, M. D.; Michelsen, K.; Hungate, R.; Gadwood, R. C.; Gaston, R. D.; Evans, B.; Mann, L. W.; Matison, M. E.; Schneider, S.; Huang, X.; Yu, D.; Andrews, P. S.; Reichelt, A.; Long, A. M.; Yakowec, P.; Yang, E. Y.; Lee, T. A.; Oliner, J. D. *J. Med. Chem.* **2009**, *52*, 7044−7053.

(16) Ding, K.; Lu, Y.; Nikolovska-Coleska, Z.; Wang, G.; Qiu, S.; Shangary, S.; Gao, W.; Qin, D.; Stuckey, J.; Krajewski, K.; Roller, P. P.; Wang, S. *J. Med. Chem.* **2006**, *49*, 3432−3435.

(17) Ding, K.; Lu, Y.; Nikolovska-Coleska, Z.; Qiu, S.; Ding, Y.; Gao, W.; Stuckey, J.; Krajewski, K.; Roller, P. P.; Tomita, Y.; Parrish, D. A.; Deschamps, J. R.; Wang, S. *J. Am. Chem. Soc.* **2005**, *127*, 10130−10131.

(18) Showalter, S. A.; Bruschweiler-Li, L.; Johnson, E.; Zhang, F.; Bruschweiler, R. *J. Am. Chem. Soc.* **2008**, *130*, 6472−6478.

(19) McCoy, M. A.; Gesell, J. J.; Senior, M. M.; Wyss, D. F. *Proc. Natl. Acad. Sci. U.S.A.* **2003**, *100*, 1645−1648.

(20) Haley, G. J.; Kong, N.; Liu, E. A.; Vu, B. T. (Hoffman-La Roche Inc.) *Preparation of chiral cis-2,4,5- triphenylimidazolines as anticancer agents.* US patent 2005/0282803 A1, December 22, 2005.

(21) Bax, A.; Grzesiek, S. *Acc. Chem. Res.* **1993**, *26*, 131−138.

(22) Kay, L. E.; Xu, G. Y.; Singer, A. U.; Muhandiram, D. R.; Formankay, J. D. *J. Magn. Reson., Ser. B* **1993**, *101*, 333−337.

(23) Delaglio, F.; Grzesiek, S.; Vuister, G. W.; Zhu, G.; Pfeifer, J.; Bax, A. *J. Biomol. NMR* **1995**, *6*, 277−293.

(24) Goddard, T. D.; Kneller, D. G. *SPARKY 3*; University of California: San Francisco, CA, 2012.

(25) Güntert, P.; Mumenthaler, C.; Wüthrich, K. *J. Mol. Biol.* **1997**, *273*, 283−298.

(26) Brunger, A. T.; Adams, P. D.; Clore, G. M.; DeLano, W. L.; Gros, P.; Grosse-Kunstleve, R. W.; Jiang, J.-S.; Kuszewski, J.; Nilges, M.; Pannu, N. S.; Read, R. J.; Rice, L. M.; Simonson, T.; Warren, G. L. *Acta Crystallogr., D* **1998**, *54*, 905−921.

(27) Laskowski, R.; Rullmann, J. A.; MacArthur, M.; Kaptein, R.; Thornton, J. *J. Biomol. NMR* **1996**, *8*, 477−486.

(28) Case, D. A.; Darden, T. A.; Cheatham, T. E.; Simmerling, C. L.; Wang, J.; Duke, R. E.; Luo, R.; Walker, R. C.; Zhang, W.; Merz, K. M.; Roberts, B.; Hayik, S.; Roitberg, A.; Seabra, G.; Swails, J.; Goetz, A. W.; Kolossvai, I.; Wong, K. F.; Paesani, F.; Vanicek, J.; Wolf, R. M.; Liu, J.; Wu, X.; Brozell, S. R.; Steinbrecher, T.; Gohlke, H.; Cai, Q.; Ye, X.; Wang, J.; Hsieh, M.-J.; Cui, G.; Roe, D. R.; Mathews, D. H.; Seetin, M. G.; Salomon-Ferrer, R.; Sagui, C.; Babin, V.; Luchko, T.; Gusarov, S.; Kovalenko, A.; Kollman, P. A. *Amber 12*; University of California: San Francisco, CA, 2012.

(29) Uhrinova, S.; Uhrin, D.; Powers, H.; Watt, K.; Zheleva, D.; Fischer, P.; McInnes, C.; Barlow, P. N. *J. Mol. Biol.* **2005**, *350*, 587−598.

(30) Zhan, C.; Varney, K.; Yuan, W.; Zhao, L.; Lu, W. *J. Am. Chem. Soc.* **2012**, *134*, 6855−6864.

(31) Doyle, M. L.; Louie, G.; Dal Monte, P. R.; Sokoloski, T. D. *Methods Enzymol.* **1995**, *259*, 183−194.

(32) Cooper, A.; Johnson, C. M.; Lakey, J. H.; Nollmann, M. *Biophys. Chem.* **2001**, *93*, 215−230.

(33) Dezi, C.; Carotti, A.; Magnani, M.; Baroni, M.; Padova, A.; Cruciani, G.; Macchiarulo, A.; Pellicciari, R. *J. Chem. Inf. Model.* **2010**, *50*, 1451−1465.

(34) Shvarts, A.; Steegenga, W. T.; Riteco, N.; van Laar, T.; Dekker, P.; Bazuine, M.; van Ham, R. C.; van der Houven van Oordt, W.; Hateboer, G.; van der Eb, A. J.; Jochemsen, A. G. *EMBO J.* **1996**, *15*, 5349−5357.

(35) Popowicz, G. M.; Czarna, A.; Rothweiler, U.; Szwagierczak, A.; Krajewski, M.; Weber, L.; Holak, T. A. *Cell Cycle* **2007**, *6*, 2386−2392.

(36) Sanchez, M. C.; Renshaw, J. G.; Davies, G.; Barlow, P. N.; Vogtherr, M. *FEBS Lett.* **2010**, *584*, 3035−3041.

(37) Joseph, T. L.; Madhumalar, A.; Brown, C. J.; Lane, D. P.; Verma, C. S. *Cell Cycle* **2010**, *9*, 1167−1181.

(38) Popowicz, G. M.; Czarna, A.; Wolf, S.; Wang, K.; Wang, W.; Domling, A.; Holak, T. A. *Cell Cycle* **2010**, *9*, 1104−1111.

(39) Phan, J.; Li, Z.; Kasprzak, A.; Li, B.; Sebti, S.; Guida, W.; Schonbrunn, E.; Chen, J. *J. Biol. Chem.* **2010**, *285*, 2174−2183.

(40) Popowicz, G. M.; Domling, A.; Holak, T. A. *Angew. Chem., Int. Ed.* **2011**, *50*, 2680−2688.

(41) Goldberg, R. N.; Kishore, N.; Lennen, R. M. *J. Phys. Chem. Ref. Data* **2002**, *31*, 231−370.